OPEN ACCESS
World Journal of Multidisciplinary Studies
ISSN (Online): 3049-0855 | Vol. 3, No. 7, July. 2026
Website: https://wasrpublication.com/index.php/wjms

Numerical Simulation and Experimental Investigation of Radar Absorbing Material for Stealth Technology

Muhammet Recep Soran[1], Ilven Mutlu[2*]

Istanbul University-Cerrahpasa, Department of Metallurgical and Materials Engineering, Istanbul 34320, Turkey.

Received: 14/05/2026 | Accepted: 02/06/2026 | Published: 20/07/2026 |

Abstract — In this study, production of radar absorption material was carried out for stealth applications in military technology. Absorbance was stuied by using a vector network analyzer (VNA), which measures the values over a frequency range and provides the results in the form of *S*-parameters. Mold filling and segregation of the epoxy matrix composite was numerically simulated and validated. The numerical simulations of the mold filling properties were carried out by using the Moldex3D in order to investigate void formation (air trap), and carbon nanotube orientation. In addition, the finite element method (FEM) based numerical simulation technique was also carried out using the ANSYS high-frequency structure simulator (HFSS) in electronic desktop in order to investigate radar absorption properties of the composites. Numerical simulation results were compared with experimental results. Distribution of the iron powders is uniform in the epoxy matrix. Increasing iron powder content increased the Young's modulus and slightly decreased the impact energy of the composite specimens. Increasing carbon nanotube content increased the Young's modulus and impact energy.

Keywords: Numercal simulation; Shielding; Composite; Radar absorption, Carbon nanotube.

1. Introduction

Electromagnetic wave absorbing materials (stealth materials) can transform electromagnetic radiation into heat through magnetic loss or dielectric loss. An ideal radar wave absorbing material should meet the requirements of low cost, strong absorption capacity, wide band-width, light-weight and small thickness [1-6].

There are magnetic loss absorption materials, which consist of magnetic powders (Ni, Fe) and polymer matrix, and dielectric loss absorption materials, which consist of conductive powders (carbon nanotube) and polymer matrix. In general, electrical permittivity and magnetical permeability are the main properties of the radar absorption materials [7-14].

Shielding effectiveness (SE) is the blocking capacity of a radar absorption material for microwaves (radar waves). It is calculated in decibels (dB) by comparing signal strength before and after adding the shield. Shielding effectiveness (SE) can be calculated by theoretical equation (1) by using absorption loss (AL), reflection loss (RL), and multiple reflection loss (ML) [15-22].

$$SE_{total} = \mathrm{AL} + \mathrm{RL} + \mathrm{ML} \quad (1)$$

Absorption loss (AL) can be calculated by equations (2), (3), and (4), where *t* is thickness, *f* is frequency, μ is the permeability (1.0 for nonmagnetic materials), σ is conductivity, δ is intrusion depth. Absorption loss (AL) is type of attenuation occurs by absorption of energy by the shielding material due to heat losses.

$$AL = 8.686\mathrm{t}\ x\sqrt{\pi f \mu \sigma} \quad (2)$$

$$AL = 20\log e^{\frac{t}{\delta}} \quad (3)$$

$$\delta = \sqrt{\frac{2}{f\mu\sigma}} \quad (4)$$

*Corresponding Author
Ilven Mutlu*
E-mail: imutlu@iuc.edu.tr.

When the radar wave passes through the material, there are multiple reflections on the interfaces between environments. If (t>>δ), impact of multiple reflections is negligible; if (t << δ) attenuation is negative and shielding effectiveness decreases.

Reflection loss (RL) indicates how much energy is reflected at the interface between the dielectric and metal barrier. Reflection loss (RL) can be calculated by equations (5) and (6). Reflection loss indicates how well the absorbing material can reduce incident electromagnetic wave. Z_o is impedance of free space. Z_s is the surface impedance.

$$RL = 20\log\frac{Z_o}{4Z_S} \quad (5)$$

$$RL = -10\log S_{11}^2 \quad (6)$$

Shielding effectiveness (SE), transmission shielding effectiveness (SE_T), reflection shielding effectiveness (SE_R), absorbtion shielding effectiveness (SE_A) parameters can be calculated by equations (7), (8), (9), and (10). Shielding effectiveness (SE) is the difference of S_{21} value with radar absorbing material and S_{21} value without radar absorbing material.

$$SE = SE'_{21} - SE_{21(RAM)} \quad (7)$$

$$SE_T = 10\log\frac{1}{S_{21}^2} \quad (8)$$

$$SE_R = -10\log(1 - |S_{21}|^2) \quad (9)$$

$$SE_A = -10 - SE_T - SE_R \quad (10)$$

Radar cross section, determines the detectability of a target by radar. Radar cross section is an area that reflects radar wave back to radar. Radar cross section depends on the target geometry, target dimensions, target material, and incline angle of the microwave. Radar cross section (σ) of the materials can be calculated by using equation (11). Radar cross section of the aircraft must be as low as possible [18-20].

$$\sigma = 10\log\left(\frac{4\pi S}{\lambda^2}\left|\frac{E_S}{E_i}\right|\right)^2 \quad (11)$$

where σ is radar cross section (dB m^2), S is the area of the model (200 mm × 200 mm), λ is the wavelength of EM, E_i is the electric field intensity of receiving waves and E_s represents the intensity of scattering waves.

In this study, production of epoxy matrix composites was carried out for radar absorbing material applications. Radar absorbing properties of composite will benefit from the dielectric loss and magnetic loss. There are several studies about the experimental production and characterization of radar absorbing polymer matrix composites. Also, there are studies about the numerical simulation of radar absorbing composites. But, there is no study on the numerical simulation and experimental investigation of the radar absorption materials (RAMs).

2. Experimental

2.1. Prouction of Epoxy Matrix Composite Radar Absorbing Material

Composite materials (radar absorption materials) were produced by using magnetic Fe powder reinforcements, electrical conductive carbon nanotube powder reinforcements, and dielectric epoxy matrix. Carbon nanotube provides electrical conduction to the radar absorption material. Single-wall-carbon nanotube (SW-CNT) with outer diameter 1.0 nm, inner diameter 0.8 nm was used. Length of carbon nanotubes was about 20 µm. Epoxy matrix was produced by using 65 wt.% epoxy prepolymer and 35 wt.% hardener. Fe powders with mean diameter of 34 µm were also added in the range of 1.0-5.0 wt.%.

2.2. Characterization Microstructure and Mechanical Properties

Mechanical properties of the polymer matrix composite specimens were determined by the tensile test device. Impact tests were carried out according to the ASTM D1709 standart by using impact fracture test device. Electrical conductivity of the composite was investigated by using WeldCheck, ETher NDE eddy current device.

2.3. Characterization of Absorbance Properties by using VNA

Absorbance and insertion loss values were measured by using a vector network analyzer (VNA), which measures the values over a frequency range. VNA provides the results in the form of *S*-parameters, such as S_{11} and S_{22} (reflection parameters), S_{21} and S_{12} (transmission parameters). Values of S_{11}, S_{12}, S_{21}, and S_{22} scattering parameters (forward reflection, forward transmission, backward transmission, reverse reflection) were determined. S_{11} parameter represents the ratio of reflected voltage at port 1 to incident voltage at port 1. Empty waveguide values were used as a reference for insertion loss (difference of S_{21} values of reference and specimen) and absorbance (difference of S_{11} values of reference and specimen) measurements. Propagation of an electromagnetic wave depends on the permittivity and permeability. Permeability is same for all ferroelectric materials, equal to free space. Permittivity depends on the composition. Measurement is based on the permittivity of material.

2.4. Numerical Simulation by using ANSYS HFSS

Finite element method (FEM) based numerical simulation technique was carried out by rectangular wave guide method using the high-frequency structure simulator (HFSS) software in ANSYS electronic desktop in order to investigate radar absorption properties. In ANSYS HFSS finite elements are in the form of tetrahedra. Entire collection of tetrahedra constitutes the finite element mesh. A solution is found for the fields within these tetrahedra. Fields are interrelated so that Maxwell's Equations are satisfied across inter-element boundaries. Once field solution is found, generalized solution is determined. HFSS considere a problem in terms of electric and magnetic fields rather than voltages and currents.

2.5. Numerical Simulation by Moldex 3D

Single-wall carbon nanotube (SWCNT) reinforced epoxy matrix composite was numerically simulated by using the Moldex3D Studio 2025R4OR in order to investigate mold filling, segregation, void formation (air trap), CNT orientation, shrinkage, filling time, welding, shear rate, powder segregation, and curing time. Disk shaped specimen with 160 mm diameter and 2 mm thickness was simulated. Solid mesh type was used in the simulation. Solid mesh element count was 1.504.099. melt and mould temperature was selected as 25 °C. Injection and curing pressure was 1 MPa. In the simulation, length to diameter ratio of the SWCNT was 3000. Content of the CNT was 0.5 wt.%.

3. Results and Discussion

3.1. Microstructure and Mechanical Properties

Magnetic particles (Fe powder) provides permeability/magnetic loss. Dielectric matrix (epoxy) provides permittvity/dielectric loss to the composite. Carbon nanotube powders provides electrical conduction. Figure 1 shows the SEM pictures of the composite at 100x and 500x magnifications. There are paths consist of carbon nanotube powders, which provide electrical conduction to the composite. Distribution of the Fe powders is uniform in the matrix.

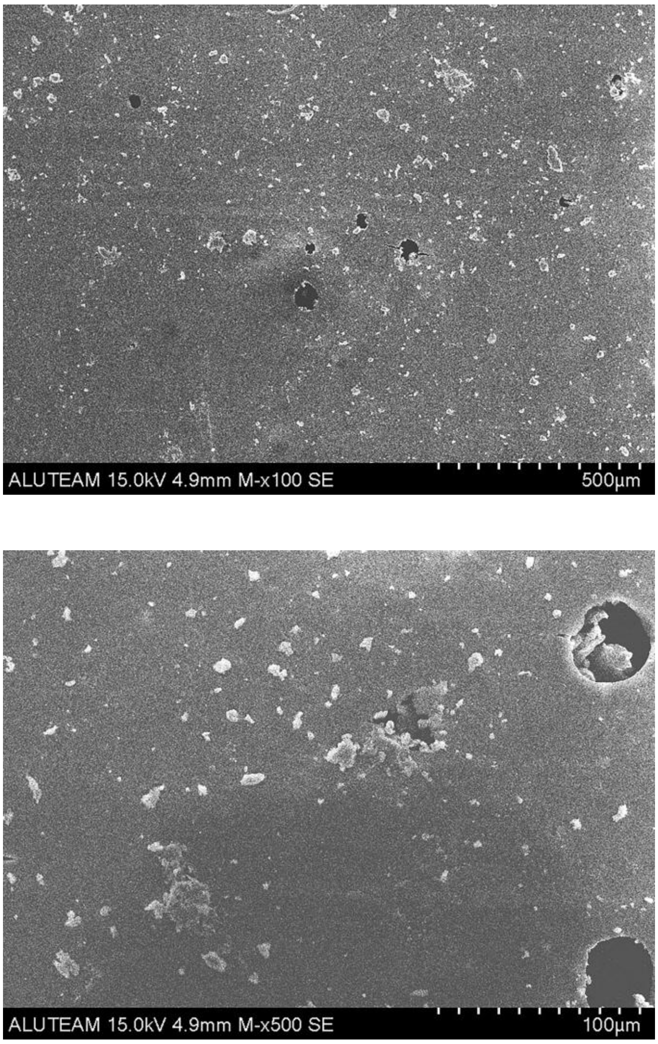

Figure 1. SEM pictures of the composite at a) 100x, and b) 500x magnifications

3.2. Physical and Mechanical Properties

Figure 2 shows the effect of carbon nanotube (CNT) content of the composites on the electrical conductivity. In general, there is a threshold (percolation zone), in which the electrical conductivity of the conductive particle filled polymer matrix composites suddenly increase from insulating zone (low conduction) to the conductive zone (high conduction).

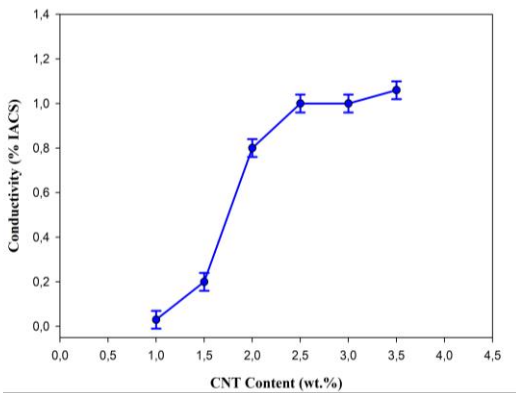

Figure 2. Effect of CNT content of the composite on the electrical conductivity

Figure 3 shows the effect of carbon nanotube (CNT) contents of the composites on the Young's modulus. Figure 4 shows the effect of carbon nanotube (CNT) contents of the composites on the impact energy.

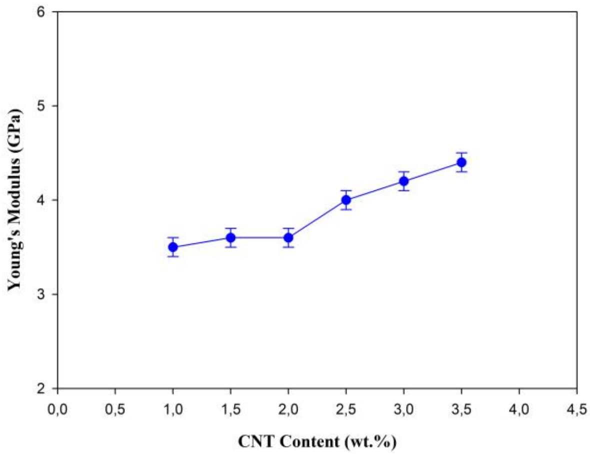

Figure 3. Effect of CNT content of the composite on the Young's modulus

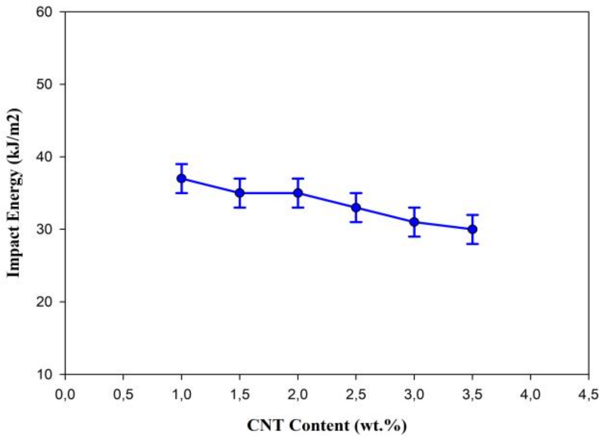

Figure 4. Effect of CNT contents of the composite on the impact energy

Figure 5 shows the effect of iron (Fe) powder content on the Young's modulus. Increasing the iron (Fe) powder content increased the Young's modulus. Figure 6 shows the effect of Fe powder content of the composites on the impact energy. Fe addition decreased the impact energy of the composites.

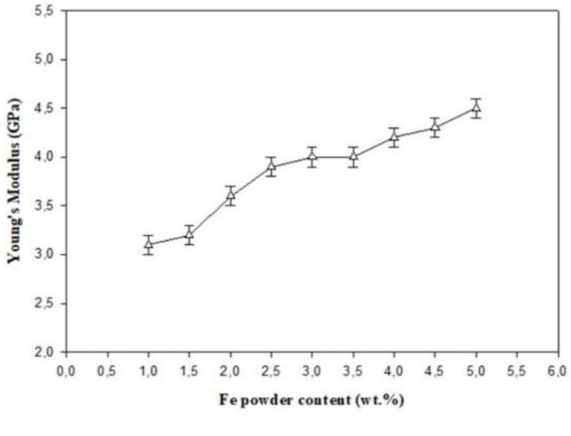

Figure 5. Effect of Fe content of the composite on Young's modulus

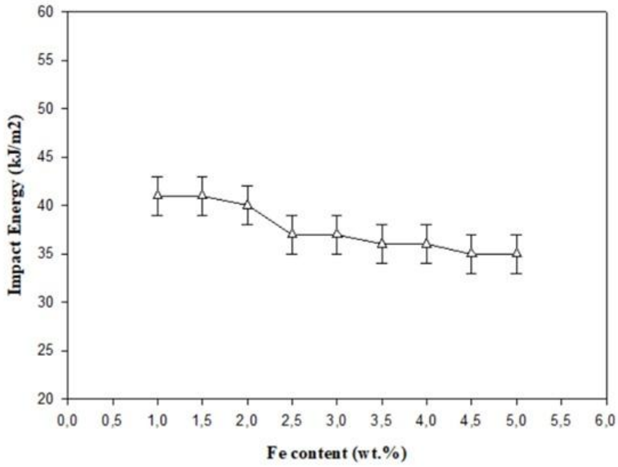

Figure 6. Effect of Fe content of the composite on the impact energy

3.3. Radar Absorption Properties Obtained by VNA

Figure 7 shows the effect of carbon nanotube (CNT) content of the composite on the absorbance. Increasing carbon nanotube contents increased the absorbance.

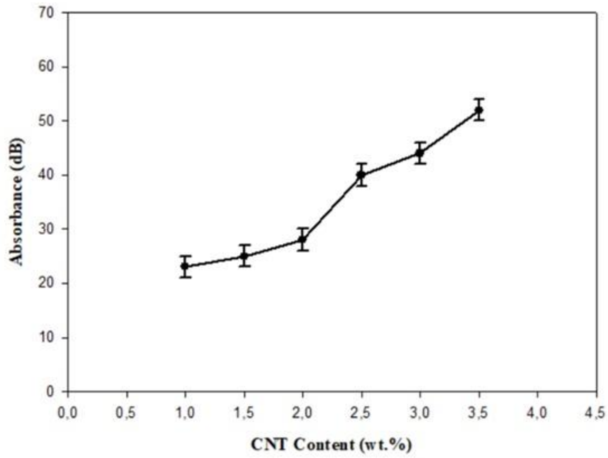

Figure 7. Effect of CNT content of the composite on the absorbance

3.4. Numerical Simulation by ANSYS HFSS

Finite element method based numerical simulation technique was carried out using the high-frequency structure simulator (HFSS) software in ANSYS electronic desktop in order to investigate radar absorption properties. Figure 8 given below shows the specimen model geometry design of the radar absorbing material and master/slave boundary conditions in the ANSYS high-frequency structure simulator (HFSS).

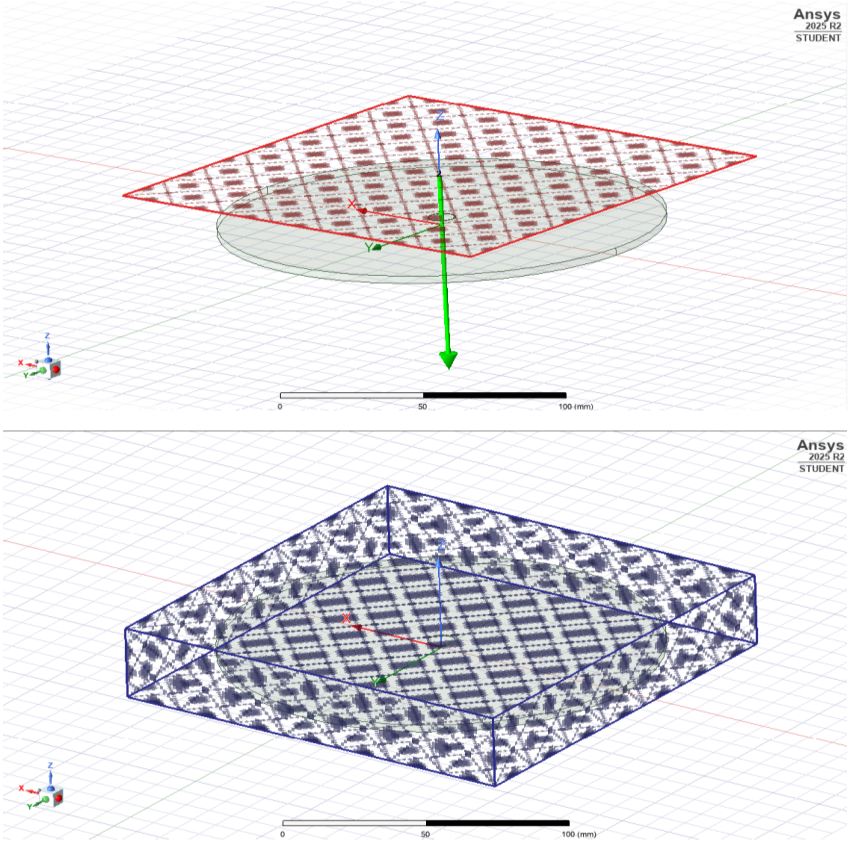

Figure 8. Specimen model design and master and slave boundary conditions in the ANSYS HFSS simulation

Figure 9 effect of frequency on the transmission coefficient of the composite in ANSYS HFSS simulation. An examination of the sweep of the composite specimens's transmission coefficient (S_{21}) in the 1–11 GHz frequency range revealed that the radar wave attenuation capacity increased in direct proportion to the rise in the material's dielectric loss tangent (tanδ). At the tanδ=0.15 value (blue curve), level dropped to -65 dB, demonstrating the most effective electromagnetic shielding. Increasing the matrix's relative permittivity from 3.2 to 4.1 (orange curve) led to resonance disruptions caused by phase mismatch, particularly in the 3.5-4.0 GHz. Results confirm that the CNT addition is critical in suppressing electromagnetic wave transmission by increasing the matrix's loss factor.

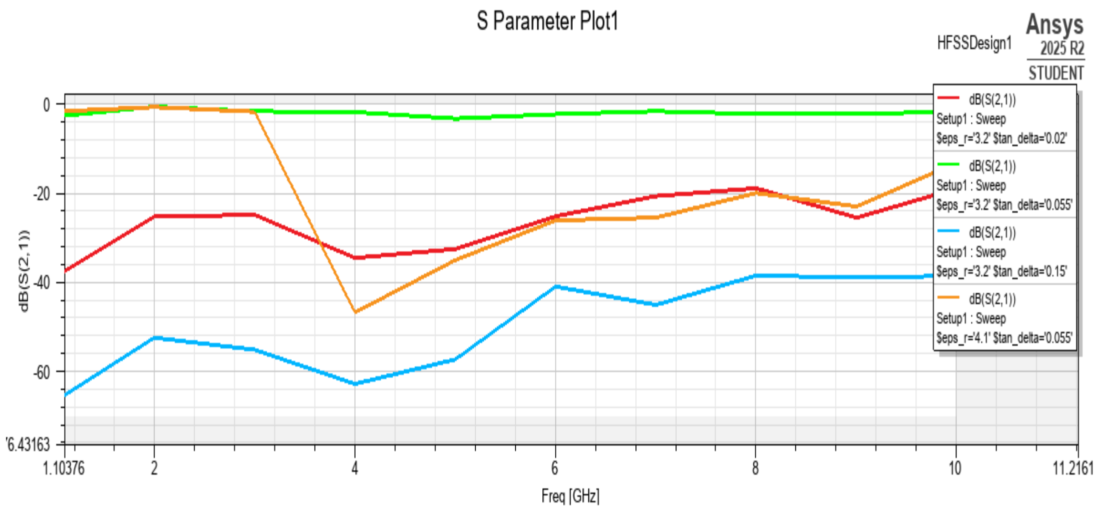

Figure 9. Effect of frequency on the transmission coefficient of the composite in ANSYS HFSS simulation

Table 1 shows the effect of CNT content and Fe content of the composite on the shielding effectiveness (SE) according to the ANSYS HFSS study. Increasing Fe content and increasing CNT contents increased the shielding effectiveness (SE) of the composite.

Table 1. Effect of CNT content and Fe content of the composite on the shielding effectiveness (SE) according to the ANSYS HFSS

Fe	**CNT (%)**				
(%)	**1**	**2**	**3**	**4**	**5**
1	20	31	33	40	56
2	30	33	35	43	60
3	36	40	42	45	62
4	40	43	45	48	63
5	45	46	49	54	65

Figure 10 shows the electric field intensity distribution on the disk-shaped composite specimen in ANSYS HFSS simulation. An examination of electric field intensity (Mag E) distribution on the disk-shaped composite specimen reveals the formation of concentric standing wave patterns within the boundaries. This annular form confirms that wave undergoes interference within the structure, triggering a cavity resonance mode. High field concentrations localized at the sample's outer periphery (149.5 V/m) are the primary physical cause of multiple side lobes observed in the far-field radiation pattern (gain plot). The drop in field intensity along the central axis aligns with the radiation null appearing along that axis. Since the electromagnetic power absorbed per unit volume in the composite structure is proportional to the square of electric field ($|E|^2$), circular regions of heightened field intensity represent the active zones where wave attenuation—and conversion of energy into heat via dielectric losses (tanδ)—occurs most effectively.

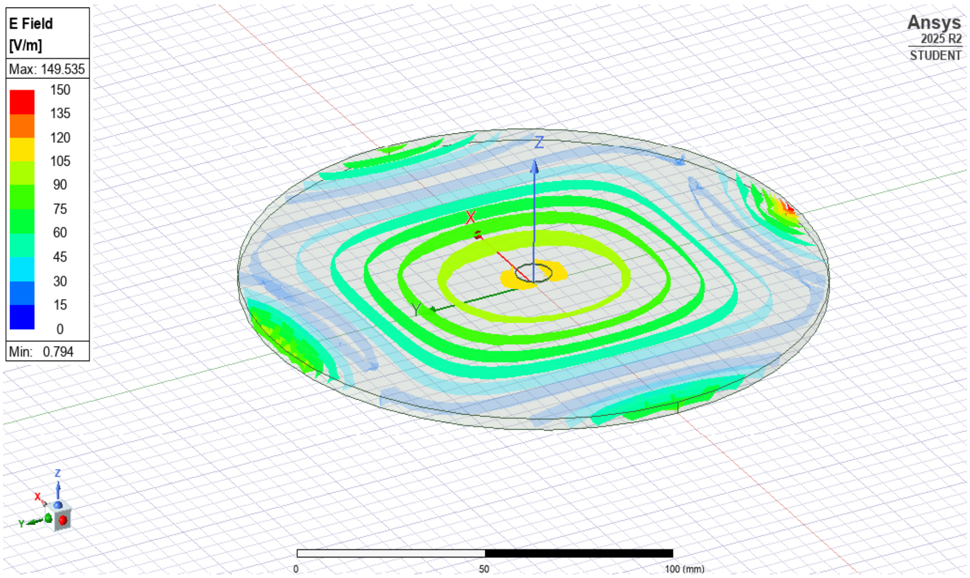

Figure 10. Electric field intensity distribution on the disk-shaped composite specimen in ANSYS HFSS simulation.

Figure 11 shows the distribution of electromagnetic power radiated from the composite specimen in ANSYS HFSS simulation. An analysis of volumetric 3D distribution (gain plot) of the electromagnetic power radiated into space from disk-shaped composite specimen reveals that the peak gain reaches a level of 7.56 dBi. Radiation pattern exhibits radial character, with majority of energy focused toward the side edges of the disk. Deep null observed along the vertical axis (passing through the center of pattern) confirms that the structure does not radiate in axial direction. The multi-lobe structure observed in the outer region results from high-order cavity resonances and circular electric field (E-field) nodes. This indicates that standing waves within the material undergo constructive interference in specific angular directions, radiating power outward.

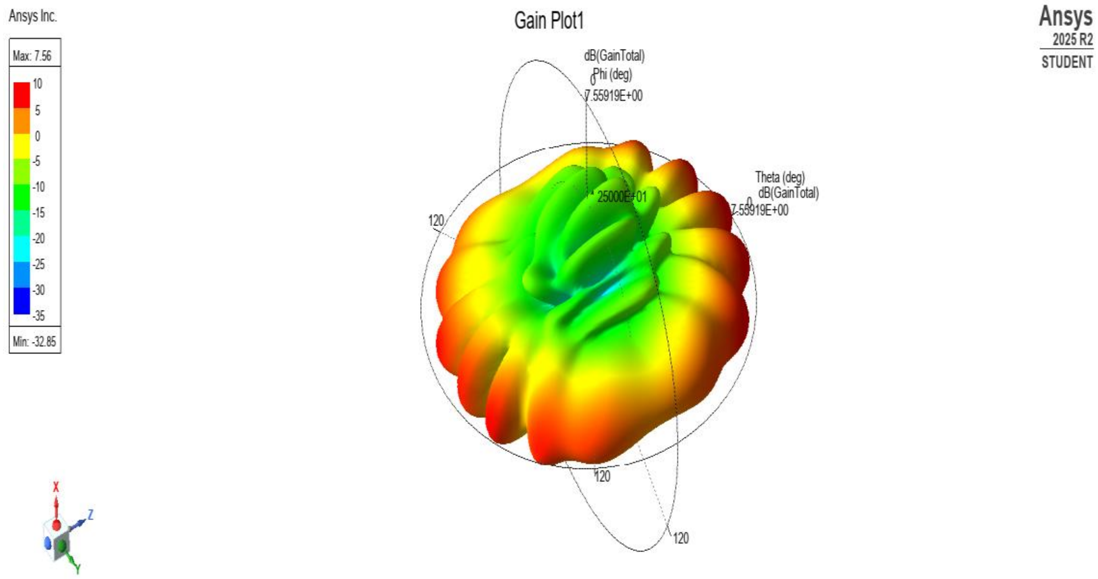

Figure 11. Distribution of electromagnetic power radiated from the composite specimen in ANSYS HFSS simulation.

Figure 12 shows the volumetric electric field map of the composite specimen in ANSYS HFSS simulation. Volumetric electric field map of the composite specimen reveals that the peak field intensity rises to 323.8 V/m in regions of local concentration. These high-field contours indicate 3D resonance hotspots within the structure and confirm the active regions where CNT-doped composite material most intensely absorbs electromagnetic waves.

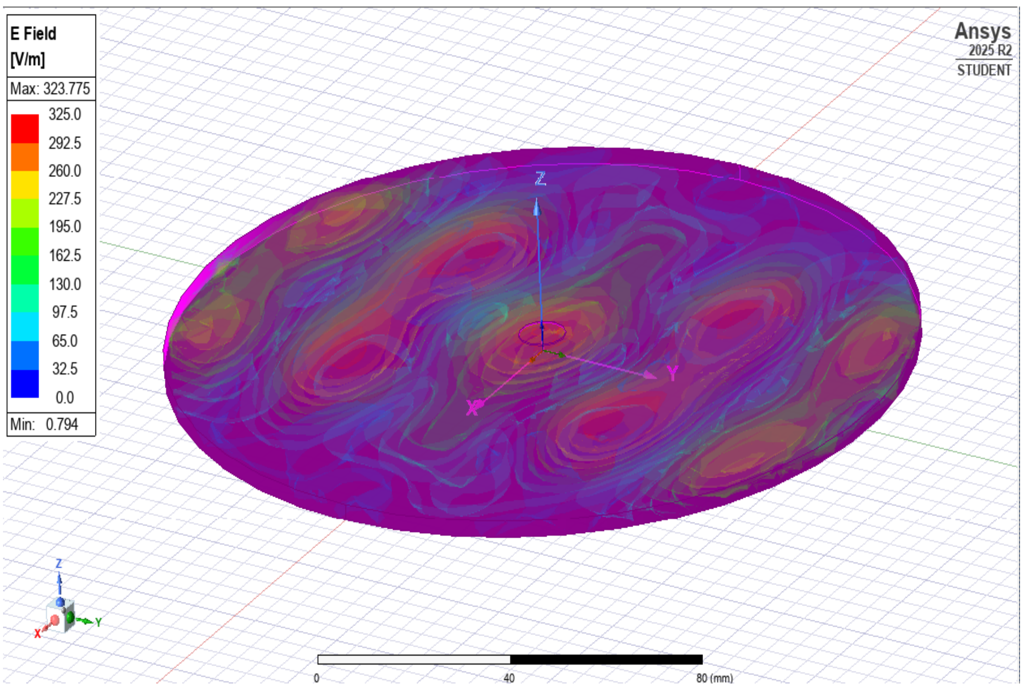

Figure 12. Volumetric electric field map of the composite specimen in ANSYS HFSS simulation.

3.5. Numerical Simulation by Moldex 3D

Carbon nanotube reinforced epoxy matrix composite was numerically simulated by using the Moldex3D Studio 2025R4OR in order to investigate mold filling, segregation, void formation (air trap), CNT orientation. Figure 13 shows the air trap simulation result of the carbon nanotube reinforced epoxy matrix composite specimen. As seen from the mage, there are some air traps at the outer edge sides of the specimen, while there are less air traps (voids) at the centre of the specimen.

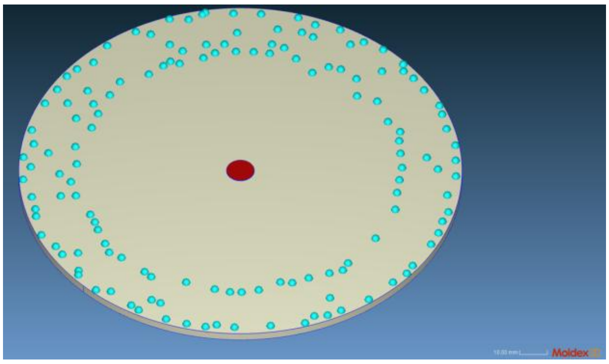

Figure 13. Air trap simulation result in Moldex 3D simulation

Figure 14 shows the (a) XX component of carbon nanotube orientation tensor in x-direction, (b) YY component of carbon nanotube orientation tensor in y-direction, and (c) ZZ component of carbon nanotube orientation tensor in z-direction.

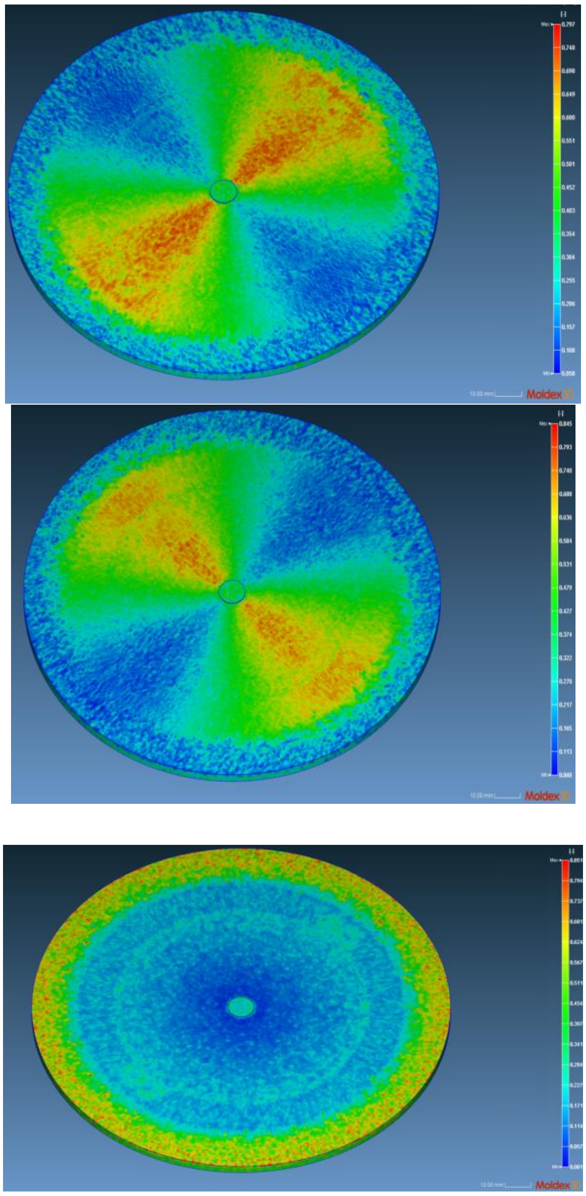

Figure 14. Carbon nanotube orientation tensors of (a) XX component in x-direction, (b) YY component in y-direction, and (c) ZZ component in z-direction in Moldex 3D simulation

Figure 15 shows the (a) vertical section of the carbon nanotube orientation, and (b) horizontal section of the carbon nanotube orientation in the epoxy matrix composite specimen. In general, distribution of the carbon nanotubes was uniform in the epoxy matrix.

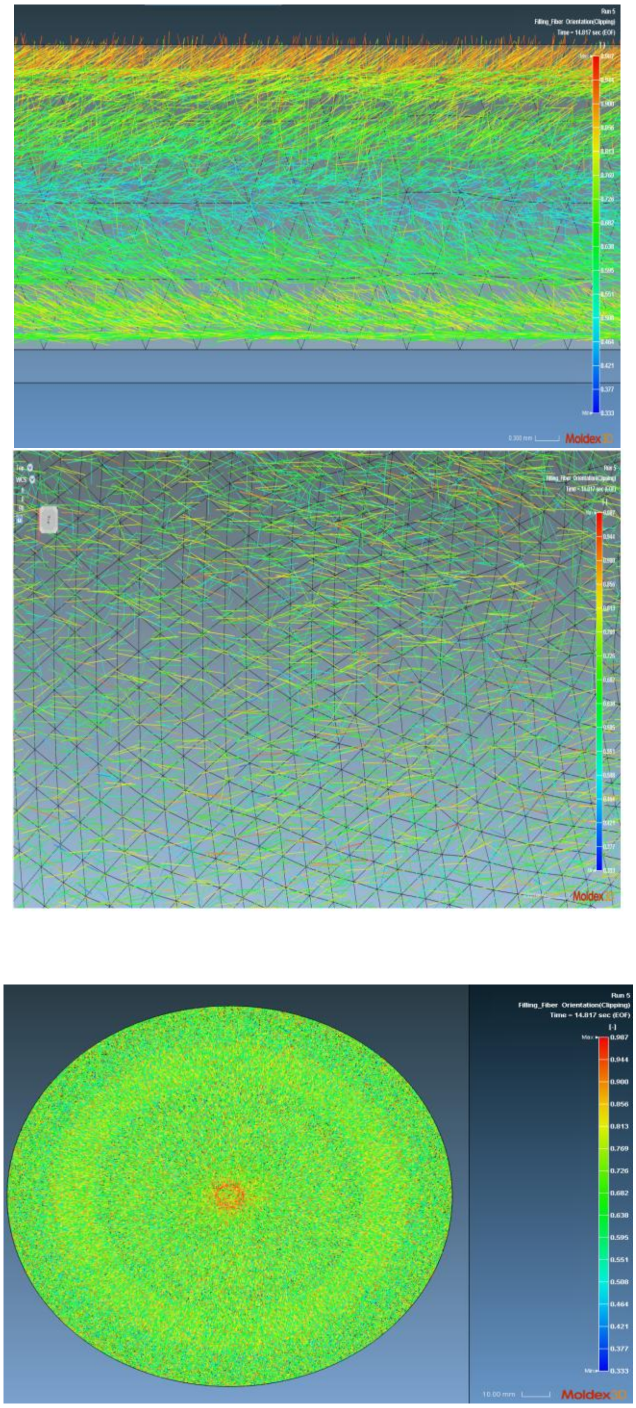

Figure 15. Carbon nanotube orientation in the epoxy matrix (a) vertical section, and (b) horizontal section in Moldex 3D simulation

4. Conclusions

The main conclusion of the study:

- Increasing the iron powder content increased the Young's modulus, while slightly decreased the impact energy level.
- Increasing carbon nanotube content increased the mechanical properties and absorbance.
- FEM based numerical simulation technique was carried out using the high-frequency structure simulator (HFSS) software in ANSYS electronic desktop in order to investigate radar absorption properties. Numerical simulation results were close to experimentan results, which were investigated by VNA.
- Carbon nanotube reinforced epoxy matrix composite was numerically simulated by using Moldex 3D software. Distribution of the carbon nanotubes was uniform in the epoxy matrix.

Acknowledgments

This work was supported by Scientific Research Projects Coordination Unit of Istanbul University-Cerrahpasa, Project Numbers of 36194 and 36358.

References

1. Song, P., Liang, C., Wang, L., Qiu, H., Gu, H., Kong, J., & Gu, J. (2019). Obviously improved electromagnetic interference shielding performances for epoxy composites via constructing honeycomb structural reduced graphene oxide. *Composites Science and Technology*, *181*, 107698.
2. Gagné, M., & Therriault, D. (2014). Lightning strike protection of composites. *Progress in Aerospace Sciences*, *64*, 1-16.
3. Yadav, R., Tirumali, M., Wang, X., Naebe, M., & Kandasubramanian, B. (2020). Polymer composite for antistatic application in aerospace. *Defence Technology*, *16*(1), 107-118.
4. Chin, W. S. (2007). Development of the composite RAS (radar absorbing structure) for the X-band frequency range. *Composite structures*, *77*(4), 457-465.
5. Wang, C., Chen, M., Lei, H., Yao, K., Li, H., Wen, W., & Fang, D. (2017). Radar stealth and mechanical properties of a broadband radar absorbing structure. *Composites Part B: Engineering*, *123*, 19-27.
6. Jayalakshmi, C. G., Inamdar, A., Anand, A., & Kandasubramanian, B. (2019). Polymer matrix composites as broadband radar absorbing structures for stealth aircrafts. *Journal of Applied Polymer Science*, *136*(14), 47241.
7. Ashraf, A., Tariq, M., Naveed, K., Kausar, A., Iqbal, Z., Khan, Z. M., & Khan, L. A. (2014). Design of carbon/glass/epoxy‐based radar absorbing composites: Microwaves attenuation properties. *Polymer Engineering & Science*, *54*(11), 2508-2514.
8. Qin, F., & Brosseau, C. (2012). A review and analysis of microwave absorption in polymer composites filled with carbonaceous particles. *Journal of applied physics*, *111*(6).
9. Kamchi, N. E., Belaabed, B., Wojkiewicz, J. L., Lamouri, S., & Lasri, T. (2013). Hybrid polyaniline/nanomagnetic particles composites: High performance materials for EMI shielding. *Journal of Applied Polymer Science*, *127*(6), 4426-4432.
10. Ozden, K., Yucedag, O. M., & Kocer, H. (2016). Metamaterial based broadband RF absorber at X-band. *AEU-International Journal of Electronics and Communications*, *70*(8), 1062-1070.
11. Thomassin, J. M., Jerome, C., Pardoen, T., Bailly, C., Huynen, I., & Detrembleur, C. (2013). Polymer/carbon based composites as electromagnetic interference (EMI) shielding materials. *Materials Science and Engineering: R: Reports*, *74*(7), 211-232.
12. Chen, X., Wu, Z., Zhang, Z., & Zou, Y. (2020). Graphene oxide aqueous solution-based metamaterial for broadband absorption. *Physica E: Low-dimensional Systems and Nanostructures*, *120*, 114017.
13. Yao, S. S., Jin, F. L., Rhee, K. Y., Hui, D., & Park, S. J. (2018). Recent advances in carbon-fiber-reinforced thermoplastic composites: A review. *Composites Part B: Engineering*, *142*, 241-250.
14. Yang, Z., Sun, X., Tian, J., Li, H., Yu, H., Wang, H., ... & Huang, Q. (2020). Broadband and polarization-insensitive microwave absorbing composite material with transmission performance based on indium tin oxide metamaterial. *Journal of Materials Science: Materials in Electronics*, *31*(16), 13838-13844.
15. Ananth, P. B., Abhiram, N., Krishna, K. H., & Nisha, M. S. (2021). Synthesis of radar absorption material for stealth application. *Materials Today: Proceedings*, *47*, 4872-4878.
16. Greety, D. B., & Wessley, J. J. (2025). Comparison of polymer materials for shielding effectiveness against electromagnetic interference and reflection losses using Ansys HFSS. *Journal of Electronic Materials*, *54*(4), 3137-3146.
17. DJ, B. G., & Wessley G, J. J. (2025). Advanced electrospun PAN–CNT nanocomposites with superior dielectric, EMI shielding, and hydrophobic performance. *Journal of Materials Science*, *60*(48), 25350-25369.

18. Chen, J., Zheng, J., Huang, Q., Wang, G., & Ji, G. (2021). Carbon fibers@ Co-ZIFs derivations composites as highly efficient electromagnetic wave absorbers. *Journal of Materials Science & Technology*, *94*, 239-246.

19. Chen, J., Zheng, J., Huang, Q., Wang, F., & Ji, G. (2021). Enhanced microwave absorbing ability of carbon fibers with embedded FeCo/CoFe2O4 nanoparticles. *ACS applied materials & interfaces*, *13*(30), 36182-36189.

20. Guo, S., Zhang, Y., Chen, J., Wu, Y., Cao, J., Tang, S., & Ji, G. (2022). The excellent electromagnetic wave absorbing properties of carbon fiber composites: the effect of metal content. *Inorganic Chemistry Frontiers*, *9*(13), 3244-3250.

21. Liu, Y., Drew, M. G., Li, H., & Liu, Y. (2020). An experimental and theoretical investigation into methods concerned with "reflection loss" for microwave absorbing materials. *Materials Chemistry and Physics*, *243*, 122624.

22. Chakradhary, V. K., Juneja, S., & Akhtar, M. J. (2020). Correlation between EMI shielding and reflection loss mechanism for carbon nanofiber/epoxy nanocomposite. *Materials Today Communications*, *25*, 101386.